



**HAL**  
open science

## Optical estimation of auroral ion upflow: Theory

M. Zettergren, J. Semeter, P.-L. Blelly, M. Diaz

► **To cite this version:**

M. Zettergren, J. Semeter, P.-L. Blelly, M. Diaz. Optical estimation of auroral ion upflow: Theory. *Journal of Geophysical Research Space Physics*, 2007, 112 (A12), pp.n/a-n/a. 10.1029/2007JA012691 . insu-03037244

**HAL Id: insu-03037244**

**<https://insu.hal.science/insu-03037244>**

Submitted on 3 Dec 2020

**HAL** is a multi-disciplinary open access archive for the deposit and dissemination of scientific research documents, whether they are published or not. The documents may come from teaching and research institutions in France or abroad, or from public or private research centers.

L'archive ouverte pluridisciplinaire **HAL**, est destinée au dépôt et à la diffusion de documents scientifiques de niveau recherche, publiés ou non, émanant des établissements d'enseignement et de recherche français ou étrangers, des laboratoires publics ou privés.

## Optical estimation of auroral ion upflow: Theory

M. Zettergren,<sup>1,2</sup> J. Semeter,<sup>1,2</sup> P.-L. Blelly,<sup>3</sup> and M. Diaz<sup>1,2</sup>

Received 27 July 2007; revised 24 August 2007; accepted 12 September 2007; published 29 December 2007.

[1] This work presents a systematic analysis of optical emissions related to auroral ion upflow. Optical intensities and field-aligned ion transport are computed for a set of monoenergetic incident electron beams using a combined fluid-kinetic model. The kinetic portion models the energetic particle transport with a multiple stream approach and provides ionization, excitation, and heating rates to an eight-moment fluid model of the ionosphere, which then calculates the resulting ion upflow. The analysis is used to develop a technique for estimating upward ion flux from photometric measurements at five discrete wavelengths: 427.8 nm, 557.7 nm, 630.0 nm, 732 nm, and 844.6 nm. The procedure involves (1) estimating the incident particle spectrum by inversion of multiwavelength optical measurements in the magnetic zenith, (2) applying this incident spectrum to the fluid-kinetic model to estimate the upflow response. The robustness of the procedure is demonstrated by inverting brightnesses computed for a known electron spectrum and then comparing upflow directly calculated from the known spectrum to the upflow calculated from the estimated spectrum. The inversion is found to provide a reliable estimate of the precipitating electron spectrum and ion upflow, even in the presence of realistic uncertainties in brightness. The technique represents a new tool for studying mass coupling between the magnetosphere and ionosphere. Potential applications range from upflow event studies to estimating the total amount of plasma entering the transition region during a substorm surge via fusion of optical data from multiple sensors.

**Citation:** Zettergren, M., J. Semeter, P.-L. Blelly, and M. Diaz (2007), Optical estimation of auroral ion upflow: Theory, *J. Geophys. Res.*, 112, A12310, doi:10.1029/2007JA012691.

### 1. Introduction

[2] Atomic oxygen ions are found in significant concentrations throughout the Earth's magnetosphere [Chappell *et al.*, 1987]. The auroral ionosphere is an important source region for magnetospheric O<sup>+</sup>, especially during geomagnetically active periods [Wilson *et al.*, 2001]. Compared to the polar wind expansion [e.g., Ganguli, 1996], auroral outflows are temporally sporadic and occur in latitudinally confined regions, concentrated near the poleward auroral boundary [Tung *et al.*, 2001; Semeter *et al.*, 2003] and arcs occurring at substorm onset [Mende *et al.*, 2003]. Because these regions may be threaded by closed field lines, the long-term impact of auroral ion outflow on the magnetospheric configuration may be significant.

[3] Several processes are known to transport ions into the magnetosphere on auroral flux tubes. Below 200 km, dissipation of the large-scale Poynting flux driving ionospheric circulation produces an outward expansion of the ionospheric plasma [Tsunoda *et al.*, 1989]. Above 200 km,

the attenuation of low-energy (<300 eV) electron precipitation serves as a topside heat source, driving electrons and ions upward via ambipolar diffusion [e.g., Richards, 1995]. These bulk thermal processes are generally referred to as "ion upflow." Above 500 km, ambient ions can be energized to escape velocity ("ion outflow") via interaction with transverse plasma waves leading to ion conic distributions [Moore *et al.*, 1999] or with the parallel electric field of the auroral acceleration region leading to ion beams [McFadden *et al.*, 1998].

[4] Because these mechanisms operate over an enormous range of temporal and spatial scale sizes, different instruments are required to observe the microphysical and macrophysical aspects of ion outflow. To date, incoherent scatter radar, sounding rockets, satellites, and computer models are widely used to study ion outflow (see reviews by Moore *et al.* [1999], Yau and André [1997], and the references therein). Incoherent scatter radar (ISR) provides low-altitude, fluid observations of ionospheric plasma during upflow events. ISR observations [Wahlund *et al.*, 1992; Forme and Fontaine, 1999; Kagan and St. Maurice, 2005] have noted the occurrence of upflow events ( $\approx 1$  km/s at 1000 km) with soft electron precipitation, high electron temperatures, and evidence of sporadic wave activity in the form of enhanced ion-acoustic echoes. Sounding rocket and satellite experiments provide an intermediate altitude snapshot of detailed microphysical processes: particle kinetics and plasma waves. These observations have noted a strong

<sup>1</sup>Department of Electrical and Computer Engineering, Boston University, Boston, Massachusetts, USA.

<sup>2</sup>Center for Space Physics, Boston University, Boston, Massachusetts, USA.

<sup>3</sup>Le Laboratoire de Physique et Chimie de l'Environnement, Le Centre National de la Recherche Scientifique, Orléans, France.

concurrency of energetic ion distributions in the presence of wave activity [André *et al.*, 1998], particle precipitation [Strangeway *et al.*, 2005], and enhanced Poynting flux [Strangeway *et al.*, 2005; Chaston *et al.*, 2006]. Satellite observations have also confirmed the correlation of soft electron precipitation and high-latitude ion upflows [Seo *et al.*, 1997; Liu *et al.*, 1995]. Combined fluid/kinetic modeling approaches have corroborated this observational evidence by showing how ionospheric convection and magnetospheric heat flows [Blelly *et al.*, 1996], precipitation [Su *et al.*, 1999; Lynch *et al.*, 2007], and wave activity [Wu *et al.*, 1999] drive the ion upflow and outflow. Further modeling efforts have demonstrated how soft precipitation, transverse wave heating, and parallel electric fields may work in concert to fuel ion outflow [Wu *et al.*, 2002; Zeng and Horwitz, 2007].

[5] The relationship of the bulk upflows observed by ISR to the energetic outflowing distributions seen by spacecraft is unclear. This is largely due to the limited geographic coverage and tight scheduling of ISR stations, which are currently the only remote diagnostic of bulk upflow. Hence few data sets exist that have the combined spacecraft-ISR observations needed to observe both the bulk upflow nature of the events and the energetic distributions of outflowing ions. This work seeks to address this shortage of combined data sets by focusing on an underutilized diagnostic for ion upflow: auroral optical emissions. Specifically, we develop a method that uses optical emissions to estimate ion upflow. An optical diagnostic for ion upflow will allow for better coverage of auroral zone upflows and more spacecraft-ground conjunctions, since it is quite feasible to establish a global chain of optical detectors. This diagnostic will help clarify the relationship of the upflow and outflow by enabling statistical studies of the combined spacecraft-ground data sets.

[6] The correlation of auroral emissions and ion upflows/outflows has been noted, qualitatively, in several papers [Hirahara *et al.*, 1998; Moen *et al.*, 2004], but these correlations have not yet been developed into a quantitative tool for studying the upflow/outflow process. We take a model-based approach to determine how optical emissions can be used as a quantitative diagnostic for studying upflow and outflow processes. A kinetic model of electron energy deposition is used to determine optical emissions and electron heating, and a fluid approach is used to capture the ionospheric upflow response. Using an eigenanalysis of the coupled fluid-kinetic models, we demonstrate the covariance of auroral optical emissions with ion upflow. We then use this analysis to formulate an inverse problem to estimate upflowing number flux from photometric measurements of selected optical emissions measured in the magnetic zenith. The accuracy and robustness of the inversion is demonstrated through simulation. Experimental validation is beyond the scope of this work and is left for a future study.

## 2. Systematic Analysis of Optical Emissions and Ion Upflow

[7] Ion upflows are observed to occur at altitudes normally above 500 km, while optical emissions are almost never observed in those regions. It is therefore necessary to justify why optical emissions can, indeed, be used to study

the higher altitude phenomena of ion upflow. Figure 1 shows a model calculation of the divergence of ion flux during an upflow event. The source region for the flux is indicated by a positive divergence which implies plasma transport away from that region. The region from 280 to 400 km has an upward and diverging flux indicating that this region is sourcing plasma to higher altitudes. Because the divergence above this region is negative or zero we can conclude that the ionosphere from 280 to 400 km sources plasma to higher altitudes during the upflow event.

[8] Also shown in Figure 1 is the optical volume emission rate at 732 nm. The plasma source region coincides quite well with the region of intense optical emissions. In fact, the upflow and optical emissions are both the effects of energy deposition by auroral electrons in this altitude region. Our technique takes advantage of this fact in order to use one effect of the energy deposition by auroral particles (optical emissions) to study another effect (ion upflow).

[9] We have chosen to use an ionospheric model, TRANSCAR, to perform our systematic analysis of auroral optical emissions and ionospheric upflow response. A detailed description of TRANSCAR is given by Lilensten and Blelly [2002], and a brief recapitulation follows. TRANSCAR is a one-dimensional time-dependent model of the ionosphere that solves for the density  $n_s$ , drift velocity  $\mathbf{u}_s$ , temperature  $T_s$ , and heat flux  $\mathbf{q}_s$  for seven different ion species ( $s = \text{O}^+, \text{H}^+, \text{N}^+, \text{N}_2^+, \text{NO}^+, \text{O}_2^+, \text{and } e^-$ ). TRANSCAR includes a fluid module which computes a numerical solution to the eight-moment equations along geomagnetic field lines and a kinetic module [Lummerzheim and Lilensten, 1994] that solves the transport equation for suprathermal electrons. The fluid and kinetic modules of TRANSCAR are dynamically coupled; at each time step the fluid module provides thermal electron density and temperature to the kinetic module and the kinetic module provides ionization, excitation, and heating rates to the fluid module. The background neutral thermospheric densities and temperatures for TRANSCAR are provided by the MSIS90 model [Hedin, 1991]. TRANSCAR is able to describe the effects of electron precipitation, which is the process of interest in this work.

[10] As an illustration of our method, Figure 2 shows a summary of the results of a set of TRANSCAR simulations modeling the effects of a set of Maxwellian auroral electron fluxes of varying characteristic energy ( $E_0$ ) on the ionosphere. The total energy flux for each simulation is fixed at  $1.4 \text{ mW/m}^2$  and is distributed isotropically in pitch angle. The figure shows that the upflow velocity (shown after 6 min exposure to precipitation) displays an inverse behavior versus energy of the precipitation, a trend previously noted in satellite observations by Seo *et al.* [1997] and in modeling work by Su *et al.* [1999]. It is also a well-known fact that optical emissions can be used as an indicator of the softness of the precipitation distribution [Rees and Lummerzheim, 1989] and therefore can be used in some sense as an indicator of upflow. In the following sections we will quantify this connection and then develop a quantitative tool for using optical emissions to estimate ion upflow.

### 2.1. Eigenanalysis Setup

[11] We will use TRANSCAR to perform simulations of the ion upflow velocities, fluxes, and the volume emissions rates of five different wavelengths: 427.8 nm, 557.7 nm,

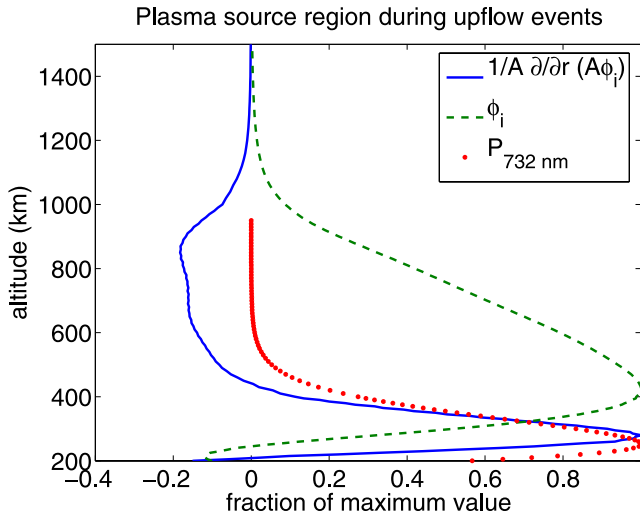
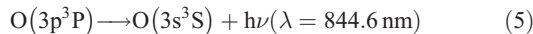
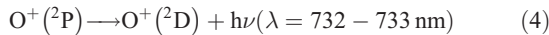
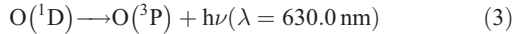
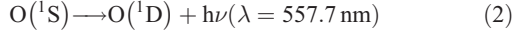
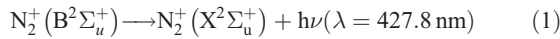


**Figure 1.** A calculation of ion flux, the divergence of the ion flux (given by  $1/A \cdot \partial/\partial r(A\phi_i)$  in a dipole coordinate system), and a volume emission rate for a simulated upflow event.

630.0 nm, 732 nm, and 844.6 nm. The transitions for these wavelengths follow.



These wavelengths were chosen because of their large signal strength, the good quantum efficiency of silicon-based detectors at these wavelengths, and the fact that these emissions are distributed over a large range of altitudes. The latter point also implies that these emissions contain information about the causative particle flux over a large range of energies. The calculations for these emission rates are not described here as they are discussed in great detail in other work [e.g., *Singh et al.*, 1996; *Semeter et al.*, 2005; *Witasse et al.*, 1999; *Torr et al.*, 1990; *Lancaster et al.*, 2000; *Borst and Zipf*, 1970, and references therein].

[12] For our systematic analysis we perform a series of simulations, each of which models the ionospheric response to a monoenergetic beam of precipitating electrons. The use of monoenergetic beams enables us to isolate which electron energies are involved in the excitation and heating processes relevant to emissions and upflow. Furthermore, monoenergetic beams at different energies serve as an orthogonal set of functions which will allow us to construct the ionospheric optical response to an arbitrary flux distri-

bution. We can therefore view the results of the simulations with this set of beams as an eigendecomposition of the ionospheric optical and upflow response. The reference intensity of the beams has been chosen so that the energy flux is a constant  $0.7 \text{ mW/m}^2$  for each beam simulation, and the discretization in energy is chosen so that there are a total of 33 logarithmically spaced energy ranges. The angular dependence of the precipitation is assumed isotropic, an assumption which may be inappropriate in some cases. However, this assumption simplifies the analysis and serves as a useful starting point for understanding the ionospheric response. Each simulation is run for 15 h before switching on the precipitation at 24 h MLT. The 15 h lead-in time insures that the results are independent of the initial state imposed on the ionosphere. Once the precipitation is switched on, it is left for an hour and then switched off. The geographic location of each simulation is set to  $65^\circ\text{N}$ ,  $147^\circ\text{W}$  (Poker Flat, AK).

## 2.2. Characteristic Ionospheric Responses

[13] A representative plot of the ionospheric response versus beam energy 5 min after each beam is switched on is shown in Figure 3. This figure shows the intensity of each ionospheric observable relative to the maximum achieved by that observable in the simulations. The upward ion flux (taken, somewhat arbitrarily, at 750 km) displays an inverse relationship to beam energy, again indicating that soft precipitation is most efficient at creating upflow. This result is well-supported in the literature [*Wahlund et al.*, 1992; *Kagan and St. Maurice*, 2005; *Lynch et al.*, 2007; *Richards*, 1995; *Seo et al.*, 1997; *Su et al.*, 1999; *Wu et al.*, 2002]. During the precipitation events the 630.0 nm line best follows the energy dependence of the upward ion flux, a trend consistent with observations by *Moen et al.* [2004] and others. This trend is expected since 630.0 nm emissions indicate energy deposition at high altitudes where upflows are initiated. The 732 nm multiplet and the 844.6 nm emission decrease in brightness with energy, while the 427.8 nm and 557.7 nm emissions increase with energy. These trends are a result of the altitude dependence of the

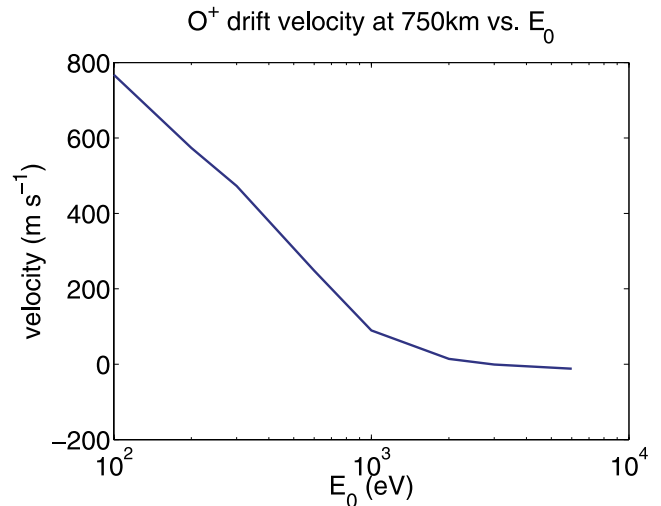


**Figure 2.** An example of how flow velocity and optical emissions vary with the precipitation distribution in energy.

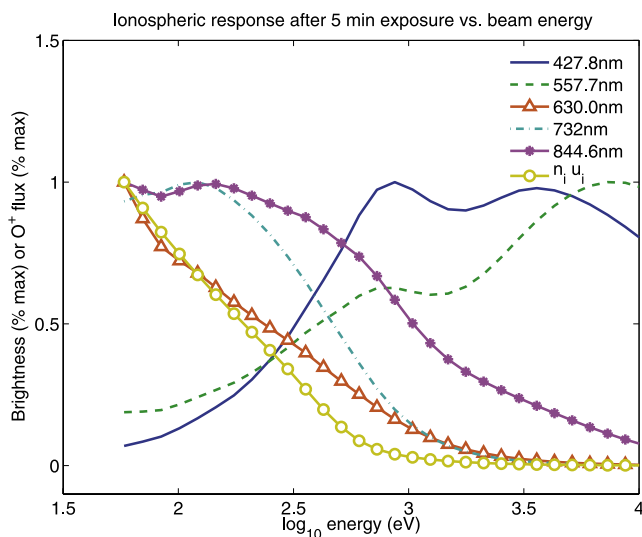


**Figure 3.** Fraction of maximum value versus beam energy for ionospheric responses after 5 min of exposure to beam precipitation. The flux ( $n_i u_i$ ) is a representative topside value taken at 750 km.

thermospheric composition: soft precipitation deposits energy in regions where O is the dominant species, creating oxygen emissions, and more energetic particles deposit energy at lower altitudes creating  $N_2$ -driven emissions. On the basis of these considerations, the 630.0 nm emission appears to be the best single emission for indicating upflow since it follows the energy dependence of the upward flux the closest. However, there are significant chemical sources for  $O(^1D)$  which can yield 630.0 nm emissions when no precipitation is present. Therefore one must be careful to subtract out the background nightglow when using this emission in inverse problems. All of the results that we will present have been corrected by having their quiescent nighttime values subtracted out. In practice this background subtraction can be accomplished by making photometric measurements in regions where no auroral emissions are present [Semeter, 2003].

[14] Figure 3 brings out another interesting property of both the optical emissions and the upflow. These quantities display a behavior that is coarsely partitioned in energy. For example, we could adequately describe the responses by dividing them into only three energy ranges: low energy (bright 630.0 nm, 732 nm, and 844.6 nm + faint 427.8 nm and 557.7 nm = intense upflow), medium energy (modest amounts of all emissions = modest upflow), and high energy (bright 427.8 nm and 557.7 nm + faint 630.0 nm, 732 nm, and 844.6 nm = no upflow). We will take advantage of this coarse partitioning later in the development of our inverse approach.

[15] Figure 4 shows the altitude and energy dependence of ionospheric plasma parameters computed from TRANSCAR after 5 min of exposure to the precipitating electron beam. For beams that produce large upward ion flux (30–500 eV), the altitude extent of the upflows can be anywhere from 300 km to greater than 1000 km (Figure 4, bottom left). Soft precipitation produces more electron heating (Figure 4, top right), which increases the polarization

electric field in the plasma. This leads to the formation of ion upflow via ambipolar diffusion. In addition, the soft precipitation creates a localized enhancement in F-region ionization (Figure 4, top right) which contributes to the polarization electric field and affects the temporal nature of the upflow, as well. If there is no significant source of F-region ionization, then electron heating alone will cause a transient upflow of plasma. This flow will redistribute the existing plasma so that the ionosphere transitions from one static equilibrium state to another. In contrast, a constant source of F-region ionization along with topside electron heating allows for a sustained upflow of plasma.

[16] Interestingly, the flux panel of Figure 4 shows that the lower-energy portion of the precipitation causes a downward flow of plasma from about 200–280 km in addition to the upflow at higher altitudes. The pressure gradients induced by the soft precipitation drives plasma downward away from the F-region. Figure 1 clearly shows that there is a small subregion of downward flow within the plasma source region that is demarcated by positive  $\nabla \cdot \phi_i$  and negative  $\phi_i$ . The downward flow is not very strong because the dense neutral atmosphere at low altitudes inhibits the flow.

[17] Figure 5 shows the altitude and energy dependence of optical emissions computed from TRANSCAR after 5 min of exposure to the same beams that drive the plasma responses of Figure 4. The emissions that result from excited or ionized forms of  $N_2$  (427.8 nm and 557.7 nm) produce emissions in the 90–150 km altitude range, while the emissions from excited or ionized forms of O (630.0 nm and 732 nm) are produced mostly in the 200–400 km altitude range. As beam energy increases the emission peaks move down in altitude since higher energy beams penetrate farther into the atmosphere. Relative to their maximum values versus energy, the 630.0 nm and 732 nm emissions decrease drastically in brightness at beam energies higher than 300 eV (Figure 3). From Figure 5 these beams create a lower altitude limit of the emission layer at 180 km for both the 630.0 nm and the 732 nm emissions. This altitude also marks the lowest point along the flux tube where there is any flow response to the precipitation (Figure 4, bottom right). This limit exists because of collisional interactions between the plasma species and the neutral background species. Below this altitude, heat input from the precipitating particles to the thermal electrons is quickly lost to the ions of the dense neutral atmosphere through a variety of inelastic cooling processes and thermalizing collisions. Furthermore, frequent collisions with the neutral species inhibit the development of any significant plasma flow. The fact that there are no 630.0 nm or 732 nm emissions below 180 km is, essentially, for the same reason that there is no upflow: collisions with the dense neutral gas quench the excited species that produce these emissions. The 427.8 nm and 557.7 nm emission dim considerably for beam energies lower than  $\approx 300$  eV (Figure 3), which corresponds to an upper altitude limit of the emission layer at 150 km (Figure 5). The 844.6 nm emission is different in the sense that it spans a large altitude and energy range (100–350 km) over the set of beam energies simulated. Because it is an oxygen emission it is excited at high altitudes, where atomic oxygen is present in relatively large concentrations. It can also be produced at lower altitudes by high energy beams

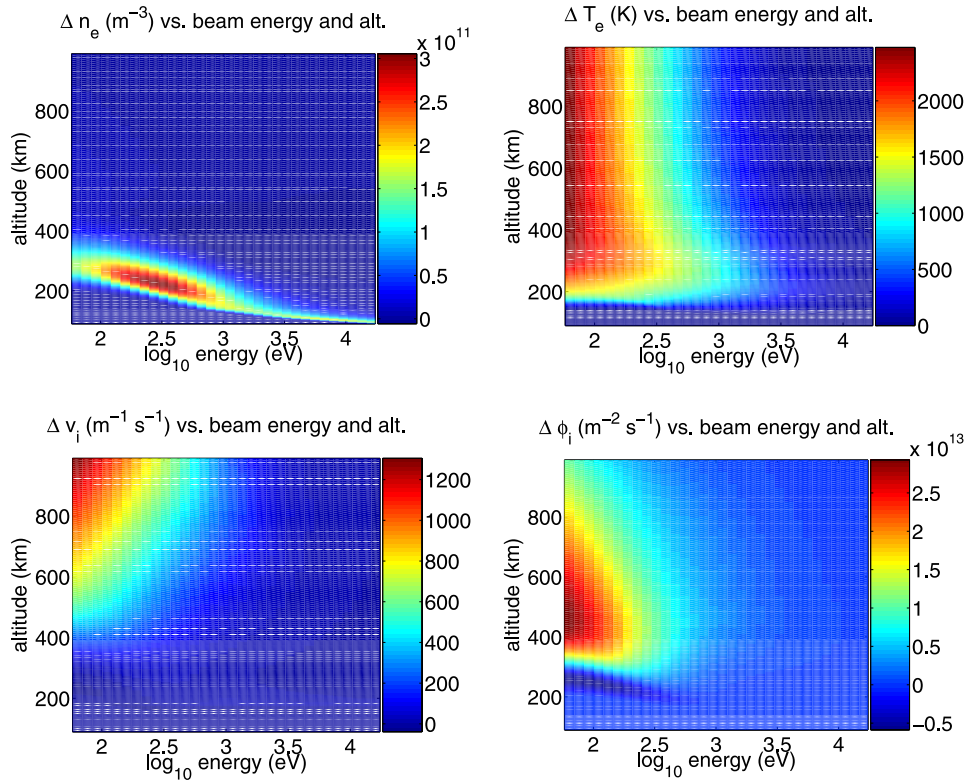


**Figure 4.** Characteristic ionospheric plasma response to monoenergetic beams in terms of electron concentration ( $n_e$ ), electron temperature ( $T_e$ ),  $O^+$  flow velocity ( $v_i$ ), and  $O^+$  flux ( $\phi_i$ ). Each plasma parameter is plotted versus beam energy and altitude. The response is captured by plotting the change in each plasma parameter due to precipitation after 5 min exposure to electron precipitation. Each beam is held at a constant total energy flux so the plots show the relative efficiency of beams at different energies in creating a response for each plasma parameter.

since it is a prompt emission which is not quenched by other thermospheric species. Furthermore, there is a minor source of 844.6 nm photons from dissociation of  $O_2$  by suprathermal electrons which contributes to this emission at low altitudes (higher beam energies).

[18] Figure 6 also shows the ionospheric response energy dependence with additional information about the temporal nature of the 630 nm emission. The response is shown immediately before, during, and immediately following a 1 h exposure to auroral electron precipitation starting at 24 h MLT ( $\approx 11.5$  h UT). The 630.0 nm emission has a temporal dependence because of the long lifetime of  $O(^1D)$ , the temperature dependent chemistry involved in producing this emission, and the dependence of the excitation process on ionospheric plasma density (see discussion section). As expected, the prompt emissions (not shown) switch on and off with the precipitation. This feature makes them better suited for studying the temporal nature of the precipitation since the prompt emissions have no chemical sources and are an instantaneous measurement of energy deposition by precipitating particles [Semeter et al., 2005].

### 3. Optical Estimator of Ion Upflow

[19] In the previous section we have presented a systematic analysis of how optical emissions and ion outflow covary with the energy distribution of precipitating elec-

trons. Our inverse approach for using optical emissions to study ion outflow involves using optical emissions to estimate the energy distribution of the precipitating electrons. The estimated electron precipitation will then be applied to a forward model of the ionosphere to estimate upflow. To accomplish this task, a forward model of the ionospheric optical and upflow response, and an inversion technique for the optical measurements is needed. As we will discuss, our systematic simulations of optical emissions from the previous section constitute a linear forward model of the ionospheric optical response and TRANSCAR itself serves as a nonlinear forward model of the upflow response. What remains is to formulate the inversion.

#### 3.1. Mathematical Formulation of Inverse Problem

[20] The rate of excitation for a species  $s$  due to collisions with electrons is

$$q_{s^*}(r) = n_s(r) \int_0^\infty \sigma_{s^*}(E) \phi(E, r) dE. \quad (6)$$

$\sigma_{s^*}$  is the cross section for electron impact excitation of species  $s$  into the excited state denoted by  $s^*$ ,  $n_s$  is the number density of the source species  $s$ , and  $r$  is the distance measured along the magnetic field line.  $\phi(E, r)$  is the suprathermal electron flux integrated over all pitch angles. For prompt emissions photon production rates can be taken

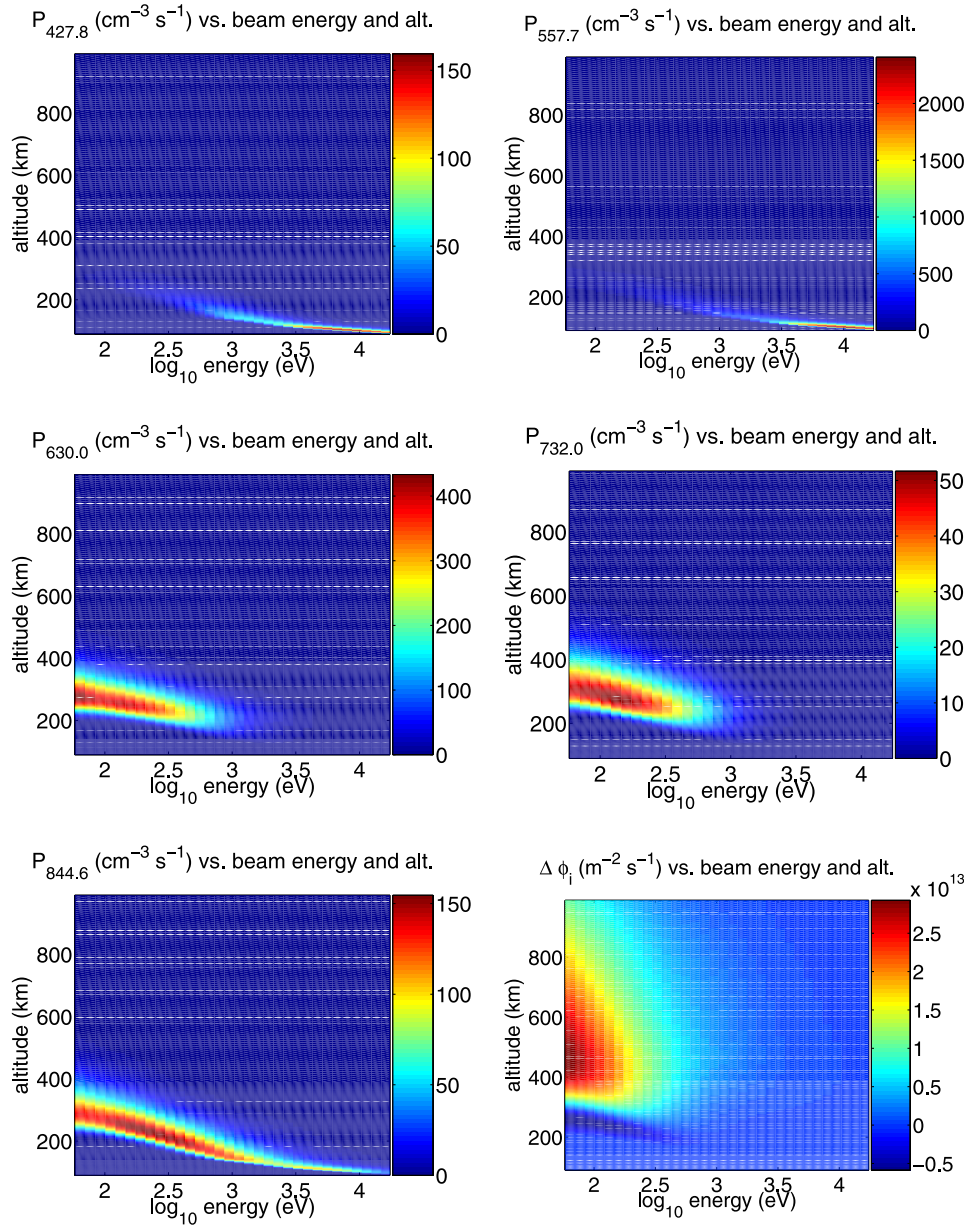


**Figure 5.** Characteristic ionospheric optical and flux response to monoenergetic beams. The volume emission rates ( $p_\lambda$ ) and  $O^+$  flux are plotted versus beam energy and altitude 5 min after the beam is switched on. Each beam is held at a constant total energy flux so the plots show the relative efficiency of beams at different energies in creating ionospheric fluxes and responses at different wavelengths. The flux panel (bottom right) is repeated here to emphasize its connection to optical emissions.

as the excitation rates. For transitions from metastable states chemical losses can be important and need to be taken into account. In this case, the concentration of the excited species ( $s^*$ ) can be calculated by assuming chemical equilibrium.

$$n_{s^*}(r) = \frac{q_{s^*}(r)}{\beta_{s^*}(r)} \quad (7)$$

where  $\beta_{s^*}$  is the loss frequency for species  $s^*$ . This equation is valid if the diffusion time constant is large compared to the time constant for chemical equilibrium, which is generally the case for the emissions and spatial scale sizes that we will

deal with. The photon volume emission rate can then be computed from the concentration as

$$p_\lambda(r) = A_\lambda n_{s^*}(r). \quad (8)$$

where  $\lambda$  is the photon wavelength and  $A_\lambda$  is the Einstein coefficient for spontaneous emission of the excited atom at wavelength  $\lambda$ . Combining equations (6), (7), and (8) the emission rate can be expressed directly in terms of the excitation source, the suprathermal electron flux.

$$p_\lambda(r) = \frac{A_\lambda}{\beta_{s^*}(r)} n_s(r) \int_0^\infty \sigma_{s^*}(E) \phi(E, r) dE. \quad (9)$$

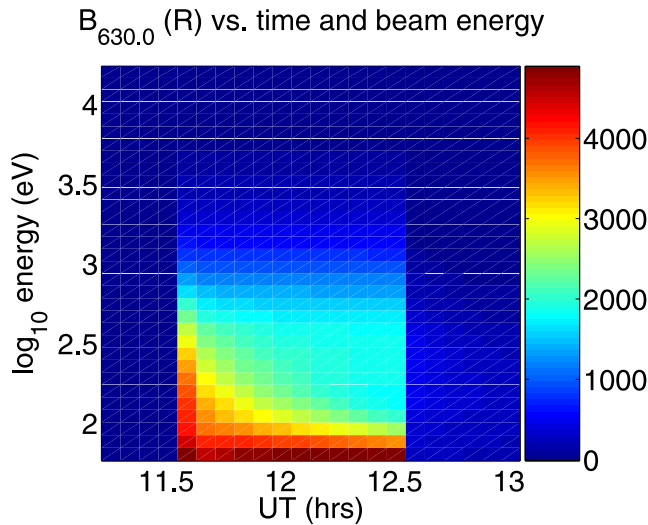


**Figure 6.** Characteristic ionospheric response to monoenergetic beams. The brightness ( $b_\lambda = \int p_\lambda dz$ ) at 630.0 nm is plotted versus time and beam energy.

Equation (9) constitutes a forward model for computing the optical volume emission rate from precipitating auroral electrons. This equation can be expressed as a Fredholm integral equation of the first kind [Semeter and Kamalabadi, 2005], an equation commonly encountered in inverse problems [Groetsch, 1993].

$$p_\lambda(r) = \int_0^\infty M_{p_\lambda}(E, r) \phi_{top}(E) dE. \quad (10)$$

In equation (10)  $M_{p_\lambda}(E, r)$  represents the forward model kernel, and  $\phi_{top}(E)$  represents the precipitating electron energy distribution at the top of the ionosphere. Because our simulations from the previous section are performed with a finite set of beams at the energies  $\{E_i\}$ , we want to use a discrete approximate of this equation.

$$p_\lambda(r) = \sum_i M_{p_\lambda}(E_i, r) \phi_{top}(E_i) \Delta E_i \quad (11)$$

The precipitating flux is therefore constructed by approximating a continuous flux distribution with a set of monoenergetic beams as illustrated in Figure 7. The resulting ionospheric optical response is simply a weighted sum of the responses to the individual beams, with the weighting factor provided by the beam intensities used to construct  $\phi_{top}(E)$ . The quantities  $M_{p_\lambda}(E_i, r) \Delta E_i$  are precisely the computations from our systematic analysis that we have shown in Figure 5.

[21] At this point we could discretize in altitude and end up with the discrete inverse problem analogous to that addressed by Semeter and Kamalabadi [2005]: using volume emission rates to estimate  $\{\phi_{top}(E_i)\}$ . This problem can be expressed in matrix form as:

$$\mathbf{p}_\lambda = \mathbf{M}_{p_\lambda} \phi. \quad (12)$$

The column vector  $\mathbf{p}_\lambda$  is the discrete form of  $p_\lambda(r)$ , the column vector  $\phi$  is the discrete form of  $\phi_{top}(E)$ , and the

matrix  $\mathbf{M}_{p_\lambda}$  is the characteristic ionospheric response shown in Figure 5. In general, it is not easy to obtain volume emission rates needed for inversion of equation (12) since optical detectors observe line-of-sight integrated brightnesses. A carefully engineered tomography experiment [e.g., Semeter *et al.*, 1999; Gustavsson, 2000] is required to convert brightnesses into the volume emission rates. Our goal here is to develop a simple diagnostic that uses easily obtainable observables (brightnesses) to predict the ion flux, so we must simplify this model further.

[22] For any particular emission wavelength, a brightness forward model can be formed by integration of both sides of equation (11) along the flux tube.

$$\int p_\lambda(r) dr = \sum_i \left[ \int M_\lambda(E_i, r) \Delta E_i dr \cdot \phi_{top}(E_i) \right] \\ b_\lambda = \mathbf{m}_\lambda^\top \phi \quad (13)$$

$b_\lambda$  represents brightness at wavelength  $\lambda$ , the column vector  $\mathbf{m}_\lambda$  represents the characteristic brightness response versus energy and  $\phi$  is again the discrete form of the precipitation distribution in energy. There is an equation of this form for each wavelength and the resulting system can be expressed in matrix form.

$$\begin{bmatrix} b_{\lambda_1} \\ b_{\lambda_2} \\ \vdots \end{bmatrix} = \begin{bmatrix} \mathbf{m}_{\lambda_1}^\top \\ \mathbf{m}_{\lambda_2}^\top \\ \vdots \end{bmatrix} \phi \\ \mathbf{b}_\lambda = \mathbf{M}_{b_\lambda} \phi \quad (14)$$

The column dimension of the matrix  $\mathbf{M}_{b_\lambda}$  captures the brightness dependence on wavelength and the row dimension captures the brightness dependence on precipitation energy. This matrix is the kernel of our discrete brightness forward model which can be inverted to estimate the

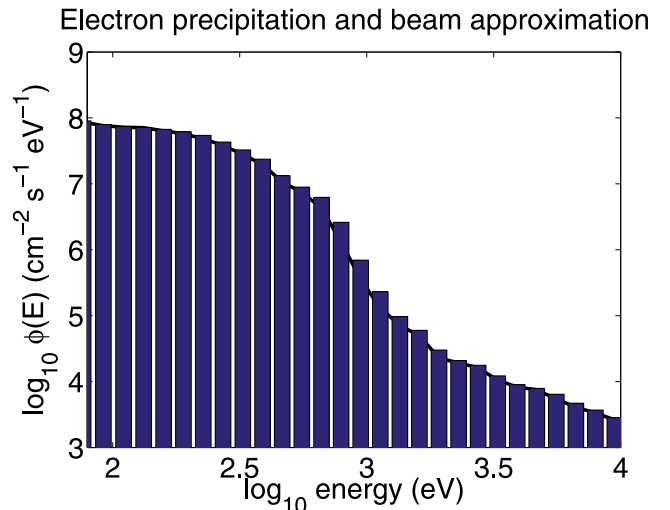


**Figure 7.** Illustration of how a continuous flux distribution is approximated by a discrete set of beams of varying intensity.

electron precipitation from measurements of brightnesses at different wavelengths.

$$\phi = \mathbf{M}_{b_\lambda}^{-1} \mathbf{b}_\lambda \quad (15)$$

In this equation,  $\mathbf{M}_{b_\lambda}^{-1}$  represents a suitable generalized inverse of  $\mathbf{M}_{b_\lambda}$ , the computation of which will be discussed later.

[23] The equations governing the upflow response of the ionosphere are the continuity, momentum, energy, and heat flux equations. These equations are listed by *Blelly and Schunk* [1993] and in many space physics textbooks. For our purpose we can express the upflow dependence on precipitation explicitly by a forward model.

$$\phi_i = f(\phi) = f(\mathbf{M}_{b_\lambda}^{-1} \mathbf{b}_\lambda) \quad (16)$$

This model gives the ion upward flux,  $\phi_i$ , from a forward model,  $f(\cdot)$ , with an input of precipitating electron flux,  $\phi$ , which is estimated from inverted brightness measurements. For our purposes  $\mathbf{M}_{b_\lambda}$  is provided by our systematic simulations and  $f(\cdot)$  is TRANSCAR's nonlinear fluid module, although we could apply this technique regardless of how these models are formulated.

### 3.2. Inversion Procedure

[24] For the inversions that we present, eight energy bins are used instead of the 33 presented in our systematic analysis. This coarse discretization may seem limiting, but the analysis presented in Figures 3 and 5 shows that the upflow and optical emissions vary slowly with energy. Furthermore, these simulations show that the upflow depends strongest on the precipitating flux below about 500 eV. Therefore if we can predict the low energy precipitating flux accurately, then we will get an accurate estimate of ion upflow. Last, a coarse energy binning has the advantage that it mitigates the ill-posed nature of the inverse problem [Groetsch, 1993].

[25] The forward model  $\mathbf{M}_{b_\lambda}$  is constructed by reforming the  $\mathbf{M}_{p_\lambda}$  matrices presented in our systematic analysis so that they contain only eight energy bins and then integrating them versus  $r$  to compute the brightnesses. As is common with inverse problems,  $\mathbf{M}_{b_\lambda}$  is poorly conditioned, which indicates that the inversion may be unstable to measurement uncertainties. Also, we have eight energy bins and only five brightness measurements so the system is underdetermined. Such problems are often handled through the use of regularization schemes [Groetsch, 1993], which incorporate prior knowledge of properties of the solution in order to reconstruct an inverse. Maximum entropy (ME) regularization has been applied to solve a similar inverse problem in the work of *Semeter and Kamalabadi* [2005] and has been shown to perform quite well in those scenarios. Qualitatively, this technique enforces a smooth (high-entropy) reconstruction of  $\phi$ , which exhibits only as much structure as can be justified from the data [Menke, 1989]. ME regularization also preserves the positivity of  $\phi$ , which is obviously desirable, and is the technique we adopt for the problem at hand. The ME regularized solution for the precipitation, denoted  $\hat{\phi}$ , is given by

$$\hat{\phi} = \min \left\{ \|\mathbf{b}_\lambda - \mathbf{M}_{b_\lambda} \phi\|^2 + \alpha \sum_i \ln(\phi_i) \right\}, \quad (17)$$

where  $\alpha$  is the regularization parameter. The solution found is therefore the one that minimizes a combination of the error norm and the negative Berg entropy [DePierro, 1991]. The minimization problem in equation 17 is solved through an iterative algorithm described by *Semeter* [1997].

[26] To illustrate our inversion scheme, we have used TRANSCAR to compute the optical brightnesses from the forward model input distribution shown in the top left of Figure 8 (the solid line). The ion upflow calculated directly from this distribution is shown in the bottom left of Figure 8 and serves as a point of comparison for evaluating the accuracy of the solution of our binned-down inverse problem. The precipitation is estimated from the TRANSCAR modeled brightnesses by using the ME regularization method to solve the inverse problem of equation (15). The top left of Figure 8 also shows an example of an inversion of noisy brightnesses (the solid line with dots). A nominal amount of zero-mean, additive white Gaussian noise ( $5.5 < \text{SNR} < 36$  depending on wavelength) was added to each brightness level to simulate a measurement. Shown in the top right of Figure 8 is the upflow calculated by using the estimated spectrum as input to our forward upflow model, TRANSCAR. The ME regularization method provides a reasonable reconstruction of the precipitation (Figure 8, top left, solid line with dots) and the estimated upflow (top right) matches the direct upflow calculation (bottom left) quite well. The difference between the actual upflow and the upflow estimated from the reconstructed distribution is shown in the bottom right of Figure 8.

[27] We have tried our inversion method on a number of different precipitation morphologies (Maxwellian, flat-top, bump-on-tail, and inverted-V) and it works well in all cases given a reasonable initial guess. As is expected with the ME regularization, inversions tend to be a bit smoother than the original distribution. Figure 9 shows an example of this. Brightnesses computed from a bump-on-tail distribution are corrupted with a nominal amount of noise as before and then inverted. In this case there is simply not enough information in the brightnesses to force the reconstruction to have as much structure as the original distribution. For us, this issue is not a problem since the soft electrons that cause upflow are observed to be distributed smoothly in energy. Indeed the low-energy portion of the distribution in Figure 9 is still recovered accurately. The degree to which the solution is smoothed can be controlled to an extent by the regularization parameter,  $\alpha$ . For the reconstructions that we have presented, we have taken  $\alpha = 1/2$  (heavy regularization). We have found that the regularization parameter should be kept as small as is needed to get a stable inversion so that as much distribution structure as possible can be recovered.

## 4. Discussion

[28] The relationship, if any, between auroral ion upflow (what we are studying) and ion outflow (beams, conics) has not been clarified. Incoherent scatter radars are the only direct remote sensing diagnostic for low-altitude ion upflow, but their geographic coverage is extremely limited, and their operations tightly scheduled. By establishing a reliable estimator of bulk ion upflow using passive optical measurements, we open an entirely new avenue for clarifying connections between low-altitude upflow and ion outflow

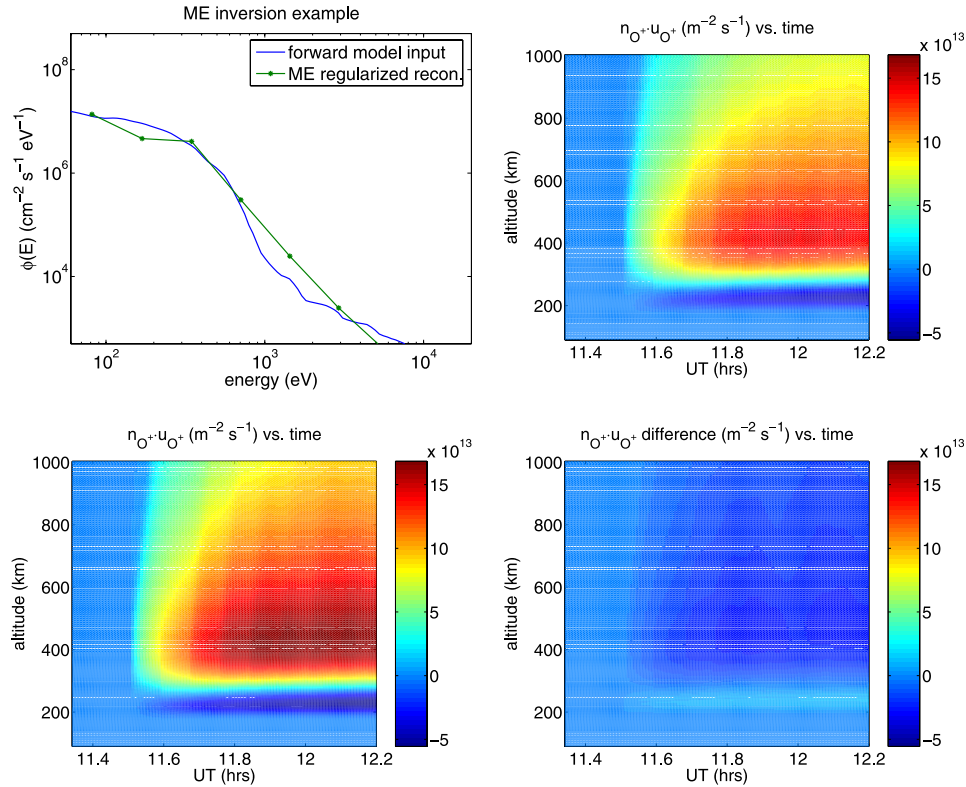


**Figure 8.** An example of an application of our optical estimator of ion upflow. Optical brightnesses are used to recover electron precipitation, and the upflow is simulated from the reconstruction. Additive white gaussian noise was added to the brightnesses computed from the actual spectrum. The SNR was between 5.5 and 36. The top two figures are the actual distribution and the reconstructed distribution (left) and the upflow calculated from the reconstructed distribution (right). The lower two figures show the upflow calculated from the actual distribution (left) and the difference between the actual upflow and the upflow calculated from the reconstructed distribution (right). The precipitation distribution used here was measured from the SIERRA sounding rocket [Klatt *et al.*, 2005; Lynch *et al.*, 2007].

to the magnetosphere. It is quite feasible to establishing a global distribution of photometers for the purpose of estimating local ion upflow characteristics. The THEMIS camera array [Craig *et al.*, 2004], for instance, serves as a prototype for such a sensor network. With such widely distributed measurements, careful planning of satellite-ground conjunctions is no longer required.

[29] The time dependence of the ionospheric upflow response is also a serious question when relating low-altitude thermal velocities to suprathermal distributions measured in the magnetosphere. The ideal experiment to resolve this outstanding question would involve simultaneous measurements of bulk ionospheric upflow (from an ISR) and particle distributions (from an in situ sensor) on a single flux tube over a period of 10's of minutes. Since such measurements are not possible, we have been left to speculate on such connections using available measurements. Here, the optical estimator also offers a fundamental advantage. With a dense enough network of sensors, simultaneous global-scale patterns of upflow may be resolved, mitigating space-time ambiguities inherent in single-point ISR measurements.

#### 4.1. Time-Dependent Considerations

[30] In our analysis we have examined the ionospheric response after 5 min exposure to the precipitating electrons.

This may seem to be a long time for the auroral zone, but in some cases it is appropriate. At the polar cap boundary we find precipitation related to Alfvén wave-particle coupling. These fluxes are also ephemeral, but they may nonetheless persist in a quasi-periodic fashion for extended periods of time. The aggregate effect will be that of a lesser stationary soft-electron flux, since the ionosphere acts as a low-pass filter with respect to plasma ionization, heating, and upwelling. Evidence for this effect is found in the narrow, columnar ionization patterns found at the poleward auroral boundary [Semeter *et al.*, 2005]. In any case, our technique does not require a steady precipitation to be accurate. It simply requires that the emissions are adequately described by time-stationary models and that we know how long to apply estimates of precipitation to the forward model of ion upflow.

[31] For prompt emissions the time-stationary forward model formulation of equations (6) and (9) applies exactly, whereas, for emissions from a state with a long lifetime it is only approximately valid. In particular, the 630.0 nm emission results from a transition of  $O(^1D)$  which has a lifetime of  $\approx 110$  s [Chamberlain, 1961]. We have calculated this emission from the time-dependent continuity equation for  $O(^1D)$ , and, accordingly, our simulations show a delay in the optical response at this wavelength. Furthermore, the buildup of F-region ionization during soft auroral precipi-

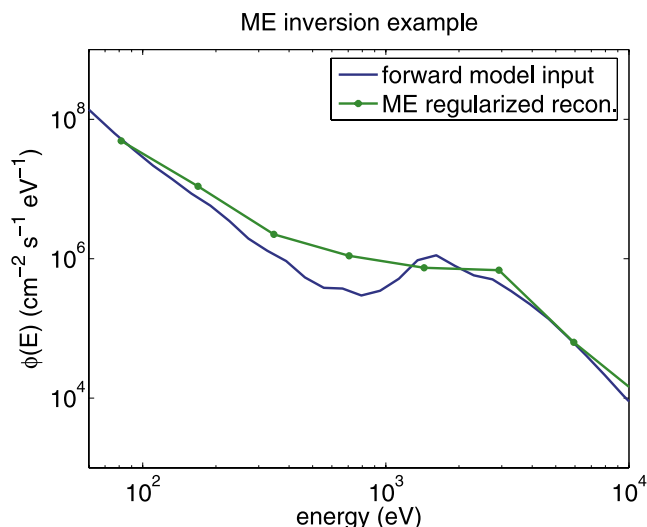


**Figure 9.** An inversion example with a bump-on-tail distribution. The ME algorithm smooths out the answer a bit but the lower energies are still recovered quite accurately.

tation has important implications for  $O(^1D)$  production and the time dependence of the 630.0 nm emission during precipitation (see Figure 6). The cross section for suprathermal electron impact production of  $O(^1D)$  is largest for electron energies below  $\approx 10$  eV [e.g., Rees, 1989, Appendix 4]. Suprathermal electrons at these energies are also responsible for most of the heat transfer to ionospheric thermal electrons [Stamnes and Rees, 1983; Rees, 1989]. F-region energy deposition by  $<10$  eV electrons is thus partitioned (roughly speaking) between the processes of  $O(^1D)$  production and thermal electron heating. The excitation rate for  $O(^1D)$  from suprathermal electron impact on O has the form of equation (6) and is proportional to atomic oxygen concentration, which is time-stationary during the electron precipitation. However, the heating rate for thermal electrons is proportional to the thermal electron concentration, which increases greatly during soft precipitation events (Figure 4, top left). This implies a shift in the partitioning of energy deposited by the suprathermal electrons. Because of the increasing thermal electron concentration, more of the energy from the suprathermals goes into heating the thermal electrons and less is available for excitation of  $O(^1D)$ . A detailed examination of  $O(^1D)$  excitation rates reveals that this is the reason for the decrease in 630.0 nm brightness with time after the initial peak (for beam energies  $>50$  eV in Figure 6). For the lowest-energy beam ( $\approx 50$  eV), the initial peak and decrease of 630.0 nm brightness versus time is, again, due to the increase in F-region ionization. However, the 630.0 nm brightness then begins to build up again for two reasons. First, the ionization increase for this beam is not as intense as for higher energy beams (Figure 4, top left), which lessens the degree of energy deposition shift away from the production of  $O(^1D)$ . Second, the electron temperature gets extremely high during the lowest energy simulation (Figure 4, top right) resulting in an increase of production of  $O(^1D)$  from thermal electron impact [Mantas and Carlson, 1991]. This mechanism is responsible for the slow buildup in time of 630.0 nm brightness (after the initial

peak and decrease) for the lowest energy beam simulation in Figure 6.

[32] On the basis of these considerations, the forward model for the 630.0 nm emission should have a small time dependence, as should any emission with chemistry involving highly time-dependent parameters (e.g.,  $n_e$ , or  $T_e$ ). Figure 6 shows that the 630.0 nm brightness has, at most, a 40–50% change over the 1 h duration of the auroral precipitation, so our time-stationary approach will still yield an approximate estimate of precipitating particle flux. The 630.0 nm emission is therefore still a far better candidate for inversion than F-region ion density, since ions have a lifetime on the order of hours at those altitudes. Previous modeling efforts [Lynch *et al.*, 2007; Zeng and Horwitz, 2007] have suggested that the upflow is not be time-stationary so we must know how long to apply to estimates of precipitation to the forward model of upflow. In fact, the prompt emissions (which are time stationary) can tell us exactly how long the auroral source persists.

#### 4.2. Other Physics

[33] The possibility of low-altitude wave-particle interactions has not been addressed in this work because we wish to isolate the effects of electron precipitation. In situ detectors find fluxes of  $<300$  eV electrons in several contexts: in the cusp/cleft, at the polar cap boundary, within inverted-V regions, at the edges of inverted-V arcs (both of the latter referred to as field-aligned bursts, or FABs, in the literature). Essentially, these fluxes are seen throughout the auroral zone.

[34] Knowledge of the thermospheric conditions may be important to correctly simulating optical emissions and outflow. The thermospheric concentrations affect the altitude distribution of energy deposition by auroral electrons, the quenching of excited species, and the ion-neutral collision frequencies that factor into ion momentum balance. The MSIS90 model that we have used provides an empirical estimate of the neutral atmosphere, and does not capture the potentially important neutral dynamics of the auroral zone. Departure of the neutral atmosphere from what was used in the simulations will introduce error into estimates of electron precipitation and upflow from the optical emissions. Ignorance of thermospheric composition could be addressed by using an indicator of thermospheric concentration ratios, similar to that in the work of Hecht *et al.* [1991]. Alternatively, we could attempt to fold the ignorance of the thermospheric concentrations into the inversion process itself to derive corrections to MSIS90 concentrations, but this is beyond the scope of the current work.

#### 4.3. Remote Sensing and Estimation

[35] This work follows in the line of other research that has been conducted on the estimation of ionospheric parameters via remote sensing. Perhaps the most closely related work is the estimation of precipitating electron spectra from optical measurements. Strickland *et al.* [1989] presented a method for using ground-based spectroscopic measurements to infer the characteristic energy and total energy flux of a parameterized distribution of precipitating electrons and correction factors to an assumed neutral atmosphere. A similar method is employed by Rees and Lummerzheim [1989] for using emissions in the visible

range to estimate the characteristic energy of the precipitating electrons. *Germany et al.* [1994a, 1994b] have studied utility of using far ultraviolet (FUV) emissions as indicators of characteristics of auroral electrons, and also for estimating ionospheric Pederson and Hall conductivities. In a similar fashion, *Aksnes et al.* [2002, 2005] has estimated ionospheric conductivities from space-based UV and X-ray observations. Recently, *Semeter et al.* [2005] has used E-region ISR plasma measurements to recover electron precipitation without any a priori assumptions about the functional form of the distribution.

[36] The work presented in this manuscript applies a technique similar to that used by *Semeter et al.* [2005] (ME regularization) to a problem like that studied by *Strickland et al.* [1989] and *Rees and Lummerzheim* [1989] (estimation of  $\phi_{top}(E)$  from optical measurements). Our resulting estimate of  $\phi_{top}(E)$  is applied to a forward model of the ionospheric response in order to estimate upflow, in a step that is similar to that applied by *Aksnes et al.* [2002] to compute the conductivities from incident energy flux. The differences between our work and previous work lies in the problem we are studying and the sophistication of the forward models and inversion techniques that we are applying. Furthermore, our technique uses different emissions to look at a different portion of the precipitating electron distribution. We focus on recovering information about the lower energy precipitating particles that are responsible for the vast majority of precipitation-driven ion upflow. Soft precipitating particles are energized by different processes than those of the auroral acceleration region, which produces higher energy distributions, and are indicative of different magnetosphere-ionosphere-thermosphere coupling processes.

## 5. Conclusions and Future Work

[37] We have presented a framework for using photometric measurements of auroral emissions to estimate field-aligned ion velocity and number flux versus altitude for flux tubes supporting auroral arc-related (type 2) ion upflows. Our formulation has been limited to line-of-sight measurements in the magnetic zenith, but the approach is readily adapted to other observing geometries. For instance, oblique measurements may be used if a tomographic inversion algorithm is incorporated into the forward model (equation (12)); nadir measurements from an orbiting platform may be used if a suitable model of Earth albedo is available and removed prior to the inversion. We could also reformulate the inverse problem itself to estimate a parameterized precipitation distribution. Alternatively, we could investigate the use of more or fewer brightnesses in the inversions. Figure 3 shows that the 732 nm and 630.0 nm emission have nearly the same characteristic versus energy, so we can likely omit one of the wavelengths and still obtain good inversions. However, the point of this paper is to present one possible technique for estimating upflow from optical emissions and to demonstrate its feasibility. Different inversions will likely be investigated in the future.

[38] The robustness and uniqueness of the proposed inversion technique has been demonstrated herein through simulation. Experimental validation of this research will be the subject of ongoing work. A simple ground-based

validation experiment involves a spectrometer, or multi-channel photometer, pointed in the magnetic zenith accompanied by simultaneous measurements of bulk ionospheric properties measured by incoherent scatter radar. Such combined radar-optical measurements are routinely made at the Sondrestrom, Greenland, ISR facility, which is located at the footpoint of the poleward auroral boundary, an ideal location for studying auroral ion upflow.

[39] **Acknowledgments.** The authors would like to thank Olivier Witasse for useful discussions. The authors would like to thank Kristina Lynch for useful advice and for supplying the data from the SIERRA flight. The authors would also like to thank Steve Capozzi and Dirk Lummerzheim for useful discussions and insight.

[40] Wolfgang Baumjohann thanks James Horwitz and Dirk Lummerzheim for their assistance in evaluating this paper.

## References

- Aksnes, A., J. Stadsnes, J. Bjordal, N. Østgaard, R. R. Vondrak, D. L. Detrick, T. J. Rosenberg, G. A. Germany, and D. Chenette (2002), Instantaneous ionospheric global conductance maps during an isolated substorm, *Ann. Geophys.*, *20*, 1181–1191.
- Aksnes, A., O. Amm, J. Stadsnes, N. Østgaard, G. A. Germany, R. R. Vondrak, and I. Sillanpää (2005), Ionospheric conductances derived from satellite measurements of auroral UV and X-ray emissions, and ground-based electromagnetic data: a comparison, *Ann. Geophys.*, *23*, 343–358.
- André, M., P. Norqvist, L. Andersson, L. Eliasson, A. I. Eriksson, L. Blomberg, R. E. Erlandson, and J. Waldemark (1998), Ion energization mechanisms at 1700 km in the auroral region, *J. Geophys. Res.*, *103*, 4199–4222.
- Blelly, P. L., and R. W. Schunk (1993), A comparative study of the time-dependent standard 8-, 13- and 16-moment transport formulations of the polar wind, *Ann. Geophys.*, *11*, 443–469.
- Blelly, P. L., A. Robineau, and D. Alcaydé (1996), Numerical modeling of intermittent outflow events above EISCAT, *J. Atmos. Terr. Phys.*, *58*, 273–285.
- Borst, W. L., and E. C. Zipf (1970), Cross section for electron-impact excitation of the (0,0) first negative band of  $N_2^+$  from threshold to 3 keV, *Phys. Rev. A*, *1*, 834–840, doi:10.1103/PhysRevA.1.834.
- Chamberlain, J. W. (1961), *Physics of the Aurora and Airglow*, AGU, Washington, D.C.
- Chappell, C. R., T. E. Moore, and J. H. Waite Jr. (1987), The ionosphere as a fully adequate source of plasma for the earth's magnetosphere, *J. Geophys. Res.*, *92*, 5896–5910.
- Chaston, C. C., V. Genot, J. W. Bonnell, C. W. Carlson, J. P. McFadden, R. E. Ergun, R. J. Strangeway, E. J. Lund, and K. J. Hwang (2006), Ionospheric erosion by Alfvén waves, *J. Geophys. Res.*, *111*, A03206, doi:10.1029/2005JA011367.
- Craig, N. G., L. Peticolas, M. Larson, S. Odenwald, C. T. Russell, S. Mende, and V. Angelopoulos (2004), THEMIS Ground-based magnetometer arrays and their education and public outreach potential, *Eos Trans. AGU*, *85*(17), Jt. Assem. Suppl., Abstract SM22A-03.
- DePiero, A. (1991), Multiplicative iterative methods in computed tomography, in *Mathematical Methods in Tomography*, edited by G. Herman, A. Louis, and F. Natterer, pp. 1441–1450, Springer, New York.
- Forme, F. R. E., and D. Fontaine (1999), Enhanced ion acoustic fluctuations and ion outflows, *Ann. Geophys.*, *17*, 182–189.
- Ganguli, S. B. (1996), The polar wind, *Rev. Geophys.*, *34*, 311–348.
- Germany, G. A., D. G. Torr, P. G. Richards, M. R. Torr, and S. John (1994a), Determination of ionospheric conductivities from FUV auroral emissions, *J. Geophys. Res.*, *99*, 23,297.
- Germany, G. A., M. R. Torr, D. G. Torr, and P. G. Richards (1994b), Use of FUV auroral emissions as diagnostic indicators, *J. Geophys. Res.*, *99*, 383–388.
- Groetsch, C. W. (1993), *Inverse Problems in the Mathematical Sciences*, Vieweg, Braunschweig.
- Gustavsson, B. (2000), Three dimensional imaging of aurora and airglow, Ph.D. thesis, Swedish Inst. of Space Phys., Kiruna.
- Hecht, J. H., A. B. Christensen, D. C. Kayser, R. L. Walterscheid, and D. J. Strickland (1991), Lower thermospheric composition changes derived from optical and radar data taken at Sondre Stromfjord during the great magnetic storm of February 1986, *J. Geophys. Res.*, *96*, 5757–5776.
- Hedin, A. E. (1991), Extension of the MSIS thermospheric model to the middle and lower atmosphere, *J. Geophys. Res.*, *96*, 1159.
- Hirahara, M., et al. (1998), Relationship of topside ionospheric ion outflows to auroral forms and precipitation, plasma waves, and convection observed by Polar, *J. Geophys. Res.*, *103*, 17,391–17,410.

- Kagan, L. M., and J.-P. St. Maurice (2005), Origin of type-2 upflows in the auroral ionosphere, *Ann. Geophys.*, *23*, 13–24.
- Klatt, E. M., P. M. Kintner, C. E. Seyler, K. Liu, E. A. MacDonald, and K. A. Lynch (2005), SIERRA observations of Alfvénic processes in the topside auroral ionosphere, *J. Geophys. Res.*, *110*, A10S12, doi:10.1029/2004JA010883.
- Lancaster, R. S., L. S. Waldrop, R. B. Kerr, J. Noto, S. C. Solomon, C. A. Tepley, R. Garcia, and J. Friedman (2000), Brightness measurements of the nighttime O I 8446 Å airglow emission from the Millstone Hill and Arecibo Observatories, *J. Geophys. Res.*, *105*, 5275–5290.
- Lilensten, J., and P.-L. Blelly (2002), The TEC and F2 parameters are tracers of the ionosphere and thermosphere, *J. Atmos. Sol. Terr. Phys.*, *64*, 775–793.
- Liu, C., J. L. Horwitz, and P. G. Richards (1995), Effects of frictional ion heating and soft-electron precipitation on high-latitude F-region upflows, *Geophys. Res. Lett.*, *22*, 2713–2716.
- Lummerzhim, D., and J. Lilensten (1994), Electron transport and energy degradation in the ionosphere: evaluation of the numerical solution, comparison with laboratory experiments and auroral observations, *Ann. Geophys.*, *12*, 83–90.
- Lynch, K. A., J. L. Semeter, M. Zettergren, P. Kintner, R. Arnoldy, E. A. MacDonald, E. Klatt, J. LaBelle, and M. Samara (2007), Auroral ion outflow: Low altitude energization, *Ann. Geophys.*, *25*, 1967–1977.
- Mantas, G. P., and H. C. Carlson (1991), Reexamination of the O(3P-1D) excitation rate by thermal electron impact, *Geophys. Res. Lett.*, *18*, 159–162.
- McFadden, J. P., et al. (1998), Spatial structure and gradients of ion beams observed by FAST, *Geophys. Res. Lett.*, *25*, 2021–2024.
- Mende, S. B., C. W. Carlson, H. U. Frey, L. M. Peticolas, and N. Østgaard (2003), FAST and IMAGE-FUV observations of a substorm onset, *J. Geophys. Res.*, *108*(A9), 1344, doi:10.1029/2002JA009787.
- Menke, W. (1989), *Geophysical Data Analysis: Discrete Inverse Theory*, Academic, San Diego, Calif.
- Moen, J., K. Oksavik, and H. C. Carlson (2004), On the relationship between ion upflow events and cusp auroral transients, *Geophys. Res. Lett.*, *31*, L11808, doi:10.1029/2004GL020129.
- Moore, T. E., R. Lundin, D. Alcayde, M. André, S. B. Ganguli, M. Temerin, and A. Yau (1999), Chapter 2-Source Processes in the High-Latitude Ionosphere, *Space Sci. Rev.*, *88*, 7–84, doi:10.1023/A:1005299616446.
- Rees, M. H. (1989), *Physics and Chemistry of the Upper Atmosphere*, Cambridge Univ. Press, Cambridge, U.K.
- Rees, M. H., and D. Lummerzheim (1989), Characteristics of auroral electron precipitation derived from optical spectroscopy, *J. Geophys. Res.*, *94*, 6799–6815.
- Richards, P. G. (1995), Effects of auroral electron precipitation on topside ion outflows, in *Cross-Scale Coupling in Space Plasma*, *Geophys. Monogr. Ser.*, vol. 93, edited by J. L. Horwitz, N. Singh, and J. L. Burch, pp. 121–126, AGU, Washington, D. C.
- Semeter, J. (1997), Ground-based tomography of atmospheric optical emissions, Ph.D. thesis, Boston Univ, Boston.
- Semeter, J. (2003), Critical comparison of OII(732–733 nm), OI(630 nm), and N<sub>2</sub>(1PG) emissions in auroral rays, *Geophys. Res. Lett.*, *30*(5), 1225, doi:10.1029/2002GL015828.
- Semeter, J., and F. Kamalabadi (2005), Determination of primary electron spectra from incoherent scatter radar measurements of the auroral E region, *Radio Sci.*, *40*, RS2006, doi:10.1029/2004RS003042.
- Semeter, J., M. Mendillo, and J. Baumgardner (1999), Multispectral tomographic imaging of the midlatitude aurora, *J. Geophys. Res.*, *104*, 24,565–24,585.
- Semeter, J., C. J. Heinselman, J. P. Thayer, and R. A. Doe (2003), Ion upflow enhanced by drifting F-region plasma structure along the night-side polar cap boundary, *Geophys. Res. Lett.*, *30*(22), 2139, doi:10.1029/2003GL017747.
- Semeter, J., C. J. Heinselman, G. G. Sivjee, H. U. Frey, and J. W. Bonnell (2005), Ionospheric response to wave-accelerated particles at the poleward auroral boundary, *J. Geophys. Res.*, *110*, A11310, doi:10.1029/2005JA011226.
- Seo, Y., J. L. Horwitz, and R. Caton (1997), Statistical relationships between high-latitude ionospheric F region/topside upflows and their drivers: DE 2 observations, *J. Geophys. Res.*, *102*, 7493.
- Singh, V., I. C. McDade, G. G. Shepherd, B. H. Solheim, and W. E. Ward (1996), The O(<sup>1</sup>S) dayglow emission as observed by the WIND imaging interferometer on the UARS, *Ann. Geophys.*, *14*, 637–646.
- Stamnes, K., and M. H. Rees (1983), Heating of thermal ionospheric electrons by suprathermal electrons, *Geophys. Res. Lett.*, *10*, 309–312.
- Strangeway, R. J., R. E. Ergun, Y.-J. Su, C. W. Carlson, and R. C. Elphic (2005), Factors controlling ionospheric outflow as observed at intermediate altitudes, *J. Geophys. Res.*, *110*, A03221, doi:10.1029/2004JA010829.
- Strickland, D. J., R. R. Meier, J. H. Hecht, and A. B. Christensen (1989), Deducing composition and incident electron spectra from ground-based auroral optical measurements. I - Theory and model results. II - A study of auroral red line processes. III - Variations in oxygen density, *J. Geophys. Res.*, *94*, 13,527–13,539.
- Su, Y.-J., R. G. Caton, J. L. Horwitz, and P. G. Richards (1999), Systematic modeling of soft-electron precipitation effects on high-latitude F region and topside ionospheric upflows, *J. Geophys. Res.*, *104*, 153–163.
- Torr, M. R., D. G. Torr, P. G. Richards, and S. P. Yung (1990), Mid- and low-latitude model of thermospheric emissions. I - O<sup>+</sup>(2P) 7320 Å and N<sub>2</sub>(<sup>2</sup>P) 3371 Å, *J. Geophys. Res.*, *95*, 21,147–21,168.
- Tsunoda, R. T., R. C. Livingston, J. F. Vickrey, R. A. Heelis, and W. B. Hanson (1989), Dayside observations of thermal-ion upwellings at 800-km altitude - An ionospheric signature of the cleft ion fountain, *J. Geophys. Res.*, *94*, 15,277–15,290.
- Tung, Y.-K., C. W. Carlson, J. P. McFadden, D. M. Klumpar, G. K. Parks, W. J. Peria, and K. Liou (2001), Auroral polar cap boundary ion conic outflow observed on FAST, *J. Geophys. Res.*, *106*, 3603–3614.
- Wahlund, J.-E., H. J. Opgenoorth, I. Häggström, K. J. Winsor, and G. O. L. Jones (1992), EISCAT observations of topside ionospheric ion outflows during auroral activity: Revisited, *J. Geophys. Res.*, *97*, 3019–3037.
- Wilson, G., D. Ober, G. Germany, and E. Lund (2001), The relationship between suprathermal heavy ion outflow and auroral electron energy deposition: Polar/Ultraviolet Imager and Fast Auroral Snapshot/Time-of-Flight Energy Angle Mass Spectrometer observations, *J. Geophys. Res.*, *106*, 18,981–18,993.
- Witasse, O., J. Lilensten, C. Lathuillère, and P.-L. Blelly (1999), Modeling the OI 630.0 and 557.7 nm thermospheric dayglow during EISCAT-WINDII coordinated measurements, *J. Geophys. Res.*, *104*, 24,639–24,665.
- Wu, X. Y., J. L. Horwitz, G. M. Estep, Y.-J. Su, D. G. Brown, P. G. Richards, and G. R. Wilson (1999), Dynamic fluid-kinetic (DyFK) modeling of auroral plasma outflow driven by soft electron precipitation and transverse ion heating, *J. Geophys. Res.*, *104*, 17,263–17,275.
- Wu, X. Y., J. L. Horwitz, G. M. Estep, Y.-J. Su, D. G. Brown, P. G. Richards, and G. R. Wilson (2002), Dynamic fluid-kinetic (DyFK) simulation of auroral ion transport: Synergistic effects of parallel potentials, transverse ion heating, and soft electron precipitation, *J. Geophys. Res.*, *107*(A10), 1283, doi:10.1029/2000JA000190.
- Yau, A. W., and M. André (1997), Sources of ion outflow in the high latitude ionosphere, *Space Sci. Rev.*, *80*, 1–25.
- Zeng, W., and J. L. Horwitz (2007), Formula representation of auroral ionospheric O<sup>+</sup> outflows based on systematic simulations with effects of soft electron precipitation and transverse ion heating, *Geophys. Res. Lett.*, *34*, L06103, doi:10.1029/2006GL028632.

P.-L. Blelly, Le Laboratoire de Physique et Chimie de l'Environnement, Le Centre National de la Recherche Scientifique, 3A, Avenue de la Recherche Scientifique, F-45071 Orléans Cedex 2, France.

M. Diaz, J. Semeter, and M. Zettergren, Department of Electrical and Computer Engineering and Center for Space Physics, Boston University, 8 St. Mary's Street, Boston, MA 02115, USA. (mattz@bu.edu)